

# Simulation of source intensity variations from atmospheric dust for solar occultation Fourier transform infrared spectroscopy at Mars



K.S. Olsen<sup>a,\*</sup>, G.C. Toon<sup>b</sup>, K. Strong<sup>a</sup>

<sup>a</sup>Department of Physics, University of Toronto, 60 St. George Street, Toronto, ON M5S 1A7, Canada

<sup>b</sup>Jet Propulsion Laboratory, California Institute of Technology, Pasadena, CA 91109, USA

## ARTICLE INFO

### Article history:

Received 30 September 2015

In revised form 25 November 2015

Accepted 30 November 2015

Available online 7 December 2015

### Keywords:

Fourier transform spectroscopy

Infrared

Source brightness fluctuations

Mars

Dust

ACE-FTS

## ABSTRACT

A Fourier transform spectrometer observing in solar occultation mode from orbit is ideally suited to detecting and characterizing vertical profiles of trace gases in the Martian atmosphere. This technique benefits from a long optical path length and high signal strength, and can have high spectral resolution. The Martian atmosphere is often subject to large quantities of suspended dust, which attenuates solar radiation along the line-of-sight. An instrument making solar occultation measurements scans the limb of the atmosphere continuously, and the optical path moves through layers of increasing or decreasing dust levels during a single interferogram acquisition, resulting in time-varying signal intensity. If uncorrected, source intensity variations (SIVs) can affect the relative depth of absorption lines, negatively impacting trace gas retrievals. We have simulated SIVs using synthetic spectra for the Martian atmosphere, and investigated different techniques to mitigate the effects of SIVs. We examined high-pass filters in the wavenumber domain, and smoothing methods in the optical path difference (OPD) domain, and conclude that using a convolution operator in the OPD domain can isolate the SIVs and be used to correct for it. We observe spectral residuals of less than 0.25% in both high- and low-dust conditions, and retrieved volume mixing ratio vertical profile differences on the order of 0.5–3% for several trace gases known to be present in the Martian atmosphere. These differences are smaller than those caused by adding realistic noise to the spectra. This work thus demonstrates that it should be possible to retrieve vertical profiles of trace gases in a dusty Martian atmosphere using solar occultation if the interferograms are corrected for the effects of dust.

© 2015 Elsevier Inc. All rights reserved.

## 1. Introduction

Solar absorption spectroscopy is affected by airborne aerosols, which absorb and scatter incoming solar radiation. These often take the form of thin clouds, water vapour, pollution, and smog. In the case of ground-based observations, these conditions may change during the day, and lead to biases in retrieved volume mixing ratios (VMRs) that may vary between measurements. While making remote sensing observations from orbit, the optical path observed by the instrument changes during acquisition, and if the line-of-sight passes through atmospheric layers with varying aerosol loading, the aerosol optical depth will change during acquisition.

The Atmospheric Chemistry Experiment Fourier Transform Spectrometer (ACE-FTS) is a high-resolution Fourier transform

spectrometer (FTS) in near-polar, low-Earth orbit on the Canadian Space Agency's (CSA's) SCISAT, launched in 2004 [1]. It operates in solar occultation geometry, measuring the absorption of solar radiation along the atmospheric limb and yielding transmission spectra using observations of the un-occulted Sun and deep space. An ACE-FTS-like instrument would be ideally suited for detecting trace gases on Mars, where the atmospheric chemistry and the existence and distribution of trace gases are not well known. ACE-FTS has a wide spectral range (750–4400  $\text{cm}^{-1}$ ), allowing it to search for dozens of trace gases active in the infrared. It has a spectral resolution of 0.02  $\text{cm}^{-1}$ , orders of magnitude better than current Mars missions [8,14], and capable of distinguishing isotopologues. Solar occultation geometry provides very high signal-to-noise ratios (SNRs) and long optical path lengths, and allows for self-calibration between each occultation.

A challenge of applying the ACE-FTS technique to the Martian atmosphere is the presence of suspended dust particles. Dust storms occur frequently on Mars, can be global in scale, and can elevate dust to altitudes above 50 km [17,9]. With ACE-FTS, the

\* Corresponding author.

E-mail addresses: [ksolsen@atmosph.physics.utoronto.ca](mailto:ksolsen@atmosph.physics.utoronto.ca) (K.S. Olsen), [geoffrey.c.toon@jpl.nasa.gov](mailto:geoffrey.c.toon@jpl.nasa.gov) (G.C. Toon), [strong@atmosph.physics.utoronto.ca](mailto:strong@atmosph.physics.utoronto.ca) (K. Strong).

treatment of interference from aerosols involves the use of retrievals from altitudes with clear skies, or specific studies of cloud properties (e.g., [7,5]) or dust events (e.g., [21,6]). However, on Mars, the extent of the dust layers can be too large to discount, while the duration of dust events can last the majority of a proposed mission length [4,14], so retrieval algorithms for an ACE-FTS-like instrument at Mars must be able to derive trace gas VMR vertical profiles from a dusty atmosphere.

Keppel-Aleks et al. [12] proposed a now-widely-used technique to mitigate the effects of source intensity variation (SIV) for instruments in the Total Carbon Column Observing Network (TCCON) [25]. The Greenhouse gases Observing SATellite (GOSAT) Thermal And Near infrared Sensor for carbon Observation (TANSO) FTS uses a similar technique [15]. Both techniques Fourier transform a raw interferogram, apply a high-pass filter, perform an inverse Fourier transform, and divide the raw interferogram by the filtered interferogram. This requires knowledge of the DC signal level and cannot be applied to AC-coupled interferograms, which are commonly recorded to satisfy the requirements of specific analog-to-digital converters (ADCs) used on the ground (e.g., [24,19]) and from orbit (e.g., [1,13]). If operating an ACE-FTS-like instrument at Mars, DC coupling will be a necessary requirement to measure and mitigate changes in the incoming solar signal.

A solar occultation instrument tracks the centre of the solar disk as the spacecraft comes out of, or enters, the shadow of the planet. During an occultation, the location and altitude of the tangent point along the optical path changes continuously. ACE-FTS uses a double pendulum swing arm with a maximum optical path difference (OPD) of  $\pm 25$  cm, and interferogram acquisition takes 2 s. How many interferograms are acquired during an occultation, and the altitude spacing between them, depends on the  $\beta$  angle (between the orbit plane and the vector from the Sun). With ACE-FTS,  $\beta$  angles between  $\pm 20^\circ$  result in a mean tangent altitude spacing between measurements of 5.5–6 km above 20 km during an occultation.

On Mars, the amount of dust along the optical path can vary significantly over the altitude range tracked during a single interferogram acquisition (1–6 km, depending on  $\beta$  angle), especially at the boundary of a dust layer. We generated synthetic spectra to simulate Mars atmospheric conditions, transformed these spectra into interferograms, and added DC signals. To simulate continuous acquisition, each interferogram was perturbed using the interferograms and DC levels of the measurements from the previous and next tangent height. We then investigated three methods to recover transmission spectra and compared them to the original synthetic spectra.

In Section 2, we describe the creation of synthetic spectra for the Mars atmosphere, their transformation into interferograms, and the SIV perturbation applied. In Section 3, we present the SIV mitigation strategies we investigated, and in Sections 4 and 5 we discuss comparisons of spectra and gas retrievals between the original synthetic spectra and those influenced by SIVs.

## 2. Simulated spectra

Synthetic transmission spectra, with a range of 850–4320  $\text{cm}^{-1}$  and resolution of 0.02  $\text{cm}^{-1}$  were generated using the GGG software suite used for analysis of spectra from the MkIV balloon-borne FTS [22] and TCCON [25]. The full spectral range is divided into two channels representing an HgCdTe (MCT) detector between 850 and 2000  $\text{cm}^{-1}$ , and an InSb detector between 1900 and 4320  $\text{cm}^{-1}$ . *A priori* profiles were developed at NASA's Jet Propulsion Laboratory (JPL), based on Viking mission results [11,16], and hypothesized trace gas quantities and vertical distributions, and include two cases for dust loading (prior to an ACE-FTS Mars

mission, these would likely be updated and incorporate global circulation model output). The vertical profiles of the mole fraction of atmospheric dust used to generate the synthetic spectra are shown in Fig. 1 for the high- and low-dust scenarios. Near the surface, the high-dust case contains around six times more dust particles, and the area most susceptible to SIVs, where the rate of change of dust loading with altitude is greatest, occurs near 60 km, compared to 20 km for the low-dust scenario. Other dust profiles were created to make stronger SIVs and are shown in Fig. 1. Two such profiles feature: (i) strong vertical stratification and (ii) a high-altitude detached layer, and are based on observations made by the Mars Climate Sounder on the Mars Reconnaissance Orbiter [17,10] and the Thermal Emission Spectrometer on Mars Global Surveyor [9]. These profiles greatly increase the rate of change of dust mole fraction with altitude, but results from their use do not differ strongly from the high-dust scenario as discussed in Section 5.

Enhanced dust produces broad spectral features characterized by a non-unity spectral baseline that varies with wavenumber. GGG uses a pseudo-line approach [23] to calculate the wavenumber-dependent attenuation due to dust from a set of laboratory-measured line strength parameters. Fig. 2 shows synthetic spectra simulating Martian atmospheric conditions for high-dust and low-dust conditions at an altitude where the rate of change of dust mole fraction is significant in both scenarios. In the high-dust case, three consecutive altitudes are shown, which illustrate the inherent problem of a real interferometer's scan beginning in the lower layer and ending in the upper layer. Also shown is a terrestrial spectrum from ACE-FTS at a similar pressure level.

These synthetic spectra are converted from transmission spectra to absorption spectra by: multiplication by the solar Planck function, addition of a Mars Planck function, and conversion of units to photons (using the field-of-view, aperture radius, throughput efficiency, integration time and spectral resolution). The spectra are multiplied by an instrument function and an efficiency function to simulate the active spectral range of the MCT and InSb detectors. Both functions were determined at JPL and based on the MkIV interferometer. The resulting spectra are then zero-filled from 0  $\text{cm}^{-1}$  to the Nyquist frequency (3235.6  $\text{cm}^{-1}$  for MCT and 6471.2  $\text{cm}^{-1}$  for InSb). Each spectrum is inverse Fourier

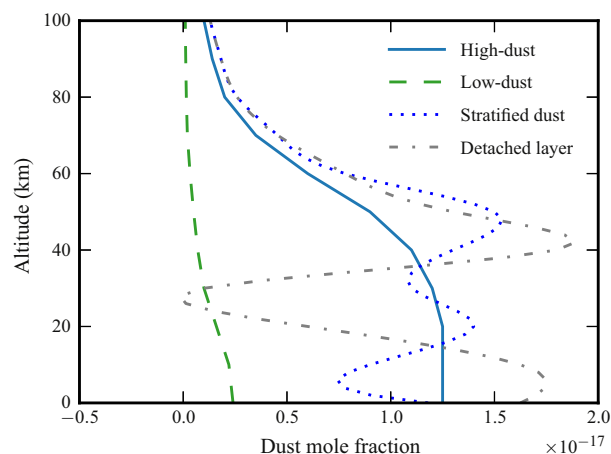


**Fig. 1.** Vertical profiles of the dust mole fraction used to generate synthetic spectra for the Martian atmosphere for high-dust (blue) and low-dust (green) conditions. The maximum rate of change of dust quantity with altitude occurs near 20 km in the low-dust case and near 60 km in the high-dust case. Also shown are scenarios that attempt to enhance the SIVs featuring strong stratification in the dust profile (grey), or detached layers of dust (grey). (For interpretation of the references to colour in this figure legend, the reader is referred to the web version of this article.)

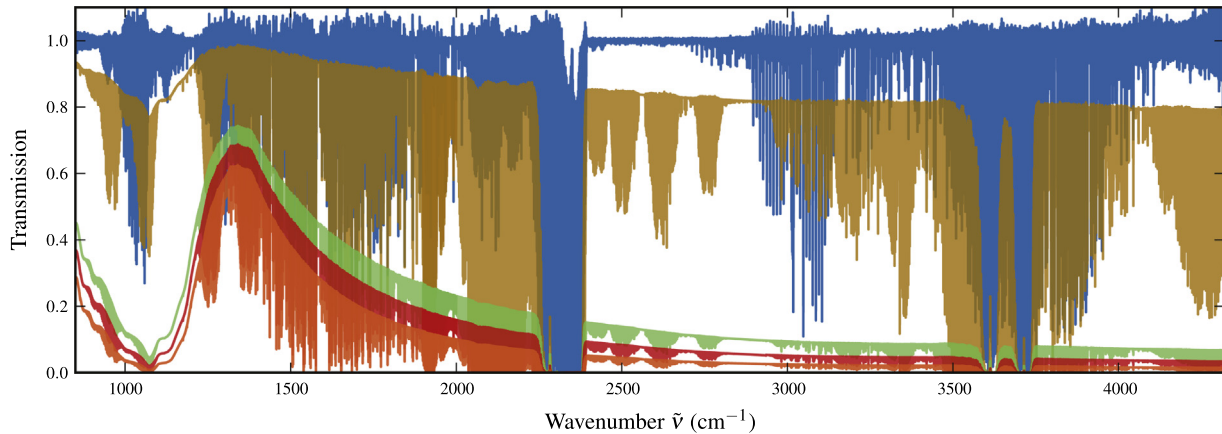


**Fig. 2.** Example spectra from an ACE-FTS-like instrument. Shown are a terrestrial spectrum recorded by ACE-FTS at 47 km (blue); a simulated Mars spectrum in low-dust conditions at 34 km (brown); a simulated Mars spectrum in high-dust conditions at 34 km (red); and the two spectra from altitudes immediately above and below the high-dust spectrum (green and orange). The tangent altitudes shown for Earth and Mars share a similar pressure of  $\sim 7.9 \times 10^{-4}$  mbar.

transformed to obtain AC interferograms from which the centreburst amplitude can be measured. A DC level,  $I_{DC}$ , is computed using the maximum and minimum of the interferogram,  $I_{max}$  and  $I_{min}$ , and the modulation efficiency, ME:

$$ME = \frac{I_{max} - I_{min}}{2I_{DC}}. \quad (1)$$

We use an ME of 80%, a realistic value obtained using the Engineering Demonstration Unit for the withdrawn Mars Atmospheric Trace Molecule Occultation Spectrometer (MATMOS) mission for the ExoMars Trace Gas Orbiter. The  $0 \text{ cm}^{-1}$  values in the spectra are replaced by  $I_{DC}$ , and can now be inverse Fourier transformed into DC interferograms.

The inclusion of dust in the spectra affects the centreburst amplitude proportionally to the amount of extinction produced, since the centreburst carries information about a spectrum's baseline level. At high altitudes, where dust levels fall off, the simulated DC interferograms all have the same centreburst amplitudes and DC levels, while at the lower altitudes centreburst amplitudes are reduced by up to 90%. Fig. 3a shows simulated interferograms for the low-dust conditions at three tangent altitudes centred at 16.5 km where the variability of dust quantity is greatest, showing the differences in centreburst amplitudes and DC levels.

To simulate SIVs, two aspects are taken into account: the DC level of the spectrometer input must vary continuously, and the intensity should change with altitude smoothly, as quantities of gas and dust vary. The interferograms created assume that the atmosphere and optical path have remained constant, and are perfectly symmetric. In reality, the optical path changes continuously as the instrument tracks the solar disk, so we must convolve each interferogram with those recorded at the tangent altitudes above,  $z_{i+1}$ , and below,  $z_{i-1}$ , it. Fixing zero OPD (ZPD) to the  $I_{DC}$  for each occultation yields a continuous, time-varying function of intensity for the entire occultation. This function, interpolated to sample points,  $x$ , and denoted  $V(x)$ , is used to weight the interferograms at  $z_{i+1}$  and  $z_{i-1}$  as:

$$wt(x, z_{i+j}) = \begin{cases} \frac{(I_{DC}(z_i) - V(x))}{(V(x) - I_{DC}(z_{i+j}))} & \text{if } x < 0 \text{ and } j = -1 \\ \frac{(V(x) - I_{DC}(z_{i+j}))}{(I_{DC}(z_i) - V(x))} & \text{if } x > 0 \text{ and } j = +1 \\ 0, & \text{otherwise} \end{cases} \quad (2)$$

where  $x$  is OPD and  $j = \pm 1$  depending on whether the weighting function will be applied to the measurement above or below. The resulting interferogram, perturbed with an SIV, is thus the weighted average of the three interferograms:

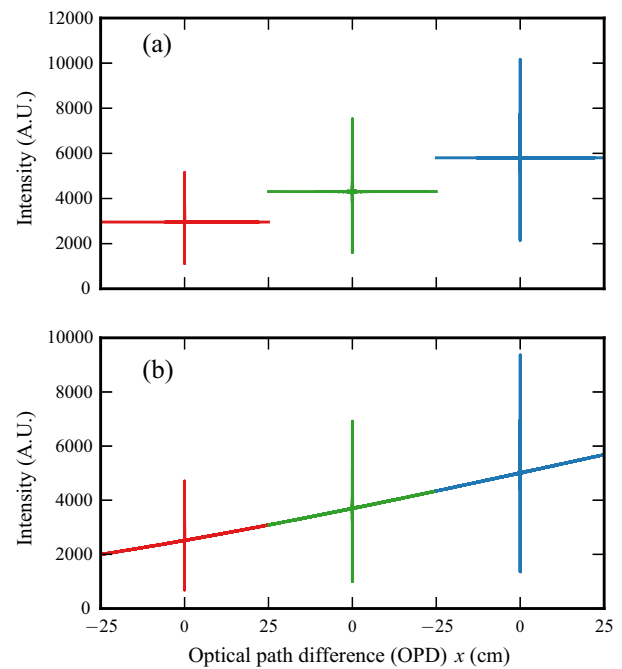


**Fig. 3.** Three consecutive simulated interferograms showing the effects of decreasing dust levels during acquisition for low-dust conditions, at altitudes of 13.6, 16.5 and 19.4 km. In (a), the interferograms have different centreburst amplitudes depending on the strength of the dust absorption, responsible for the baseline level in Fig. 2, and DC levels computed from Eq. (1). In (b), the maximum OPD regions have been mixed with the symmetric interferograms from altitudes above and below, and the DC level has been forced to vary continuously.

$$I_{SIV}(x, z_i) = \frac{wt(x, z_{i-1})I(x, z_{i-1}) + I(x, z_i) + wt(x, z_{i+1})I(x, z_{i+1})}{wt(x, z_{i-1}) + 1 + wt(x, z_{i+1})}. \quad (3)$$

This gives approximately even weights between the current layer and those above or below at maximum OPD, while leaving ZPD unaffected. Fig. 3b shows the interferograms from Fig. 3a now perturbed with an SIV.

### 3. Mitigation

The strategy to mitigate SIVs, originally suggested by Brault [3], is to obtain a smooth function with which to re-weight the interferogram as:

$$I_{\text{corr}}(x) = \frac{I_{\text{SIV}}(x)}{I_{\text{smooth}}(x)}. \quad (4)$$

The resulting  $I_{\text{corr}}(x)$  will have a constant DC level of 1, preserving spectral information in the centreburst and high-OPD wings, but requiring re-normalization. We examined three methods to obtain  $I_{\text{smooth}}(x)$ :

- (i) using the known  $V(x)$  as  $I_{\text{smooth}}(x)$ ,
- (ii) obtaining  $I_{\text{smooth}}(x)$  by high-pass filtering  $I_{\text{SIV}}(x)$  in the wavenumber domain as in Keppel-Aleks et al. [12],
- (iii) applying a convolution operator to  $I_{\text{SIV}}(x)$  to obtain  $I_{\text{smooth}}(x)$ .

Method (i) simply removes the known DC level without taking into account perturbations caused by mixing the interferogram with adjacent altitudes. This is used as the baseline case, representing no correction.

Method (ii) refers to the following filter suggested by Keppel-Aleks et al. [12]:

$$f(\tilde{\nu}) = \begin{cases} \left( \frac{1 + \cos \pi \tilde{\nu} / s}{2} \right)^N, & \text{if } \tilde{\nu} < s, \\ 0, & \text{if } \tilde{\nu} > s, \end{cases} \quad (5)$$

where  $s = 300 \text{ cm}^{-1}$  is the wavenumber cutoff, and  $N = 8$  controls the cutoff steepness. The interferograms in Fig. 3b cannot be usefully Fourier transformed without any treatment since the slope of the baseline results in a spectrum containing the transform of a linear function. This is not confined to low-wavenumbers, but interferes throughout the entire wavenumber range. Thus, high-pass filtering  $\tilde{T}_{\text{SIV}}(\tilde{\nu})$  to obtain  $I_{\text{smooth}}(x)$  insufficiently mitigates SIVs (where  $\tilde{T}(\tilde{\nu})$  represents the Fourier transform of  $I(x)$ ). The resulting  $I_{\text{smooth}}(x)$  has large perturbations at maximum OPD that must undergo an additional step constraining the endpoints to  $V(x)$  in the OPD domain to obtain a corrected spectrum.

The convolution operator in Method (iii) is that by used the slice-ipp software, a fast Fourier transform algorithm developed at JPL and used by TCCON. It is meant to be the OPD-domain equivalent to the high-pass filter presented in Keppel-Aleks et al. [12], and is the result of that work. To perform a high-pass filter in the OPD domain, the OPD-domain interferogram is convolved with the inverse Fourier transform of an appropriate wavenumber-domain filter function. In slice-ipp, the function convolved with an interferogram is given by:

$$F(x) = \frac{\sin(2sx\pi)}{2sx\pi} + \frac{1}{2} \left( \frac{\sin(2sx\pi + \pi)}{2sx\pi + \pi} + \frac{\sin(2sx\pi - \pi)}{2sx\pi - \pi} \right), \quad (6)$$

and  $I_{\text{smooth}}(x) = I_{\text{SIV}}(x) * F(x)$ . The wavenumber cutoff,  $s$ , is higher in the slice-ipp method, close to the lower bound of the wavenumber range of the detector, and the cutoff steepness is less sharp than the original high-pass filter of Keppel-Aleks et al. [12]. Near zero OPD, where the centreburst amplitude is largest,  $I_{\text{smooth}}(x)$  requires an additional smoothing step to reduce its amplitude. Practical advantages of applying the filter in the OPD domain are computational simplicity and efficiency, since it can be done with shorter operators and does not require calling a fast Fourier transform subroutine.

Other methods of smoothing  $I_{\text{SIV}}(x)$ , such as using a moving average, an exponential filter, and a Savitzky–Golay filter, were investigated. These either left artifacts at maximum OPD that lead to interference in the detector wavenumber range, or leave too much low-amplitude structure from  $I_{\text{SIV}}(x)$  in  $I_{\text{smooth}}(x)$ , resulting in changes to absorption line relative depths. Other forms of a high-pass filter in the wavenumber domain suffer from the same inherent problem with the simulated SIVs described above.

Renormalization is done by multiplying the DC interferogram,  $I_{\text{corr}}(x)$ , by the ZPD level of the smoothed function,  $I_{\text{smooth}}(x)$ . The

interferograms are then Fourier transformed, phase corrected in the wavenumber domain using the Mertz method [18], and the reverse of the steps in Section 2 are performed to obtain transmission spectra.

## 4. Results

### 4.1. Spectra

The effects of the SIV perturbation are shown in Fig. 4. The top panel shows the maximum OPD regions of an interferogram with the  $+25 \text{ cm}^{-1}$  region's  $x$ -axis reversed. This interferogram has been corrected using only the known  $V(x)$ , such that the  $-25 \text{ cm}^{-1}$  region and the  $+25 \text{ cm}^{-1}$  have the same DC level. This illustrates the magnitude of the asymmetry caused by perturbing the interferograms with those from altitudes above and below, simulating interferogram acquisition beginning in a different optical layer than it ends in, with different gas and dust quantities. The bottom panel shows the low-wavenumber region of the resulting spectrum. Prior to simulating an SIV, this region of the spectrum was zero-filled; all the structure has been caused by the SIV simulation. The filter presented in Keppel-Aleks et al. [12] would leave only the signal in this region to produce  $I_{\text{smooth}}(x)$ . The interferogram and corresponding spectrum shown are from 19.4 km in low-dust conditions, the same conditions as in Fig. 3.

A sequence of 64 spectra from 2 to 167 km were created for low- and high-dust conditions, and each one was transformed into an interferogram and had the SIV perturbation applied. Each of the mitigation strategies were applied to produce three sets of transmission spectra over the wavenumber range of the MCT and InSb detectors.

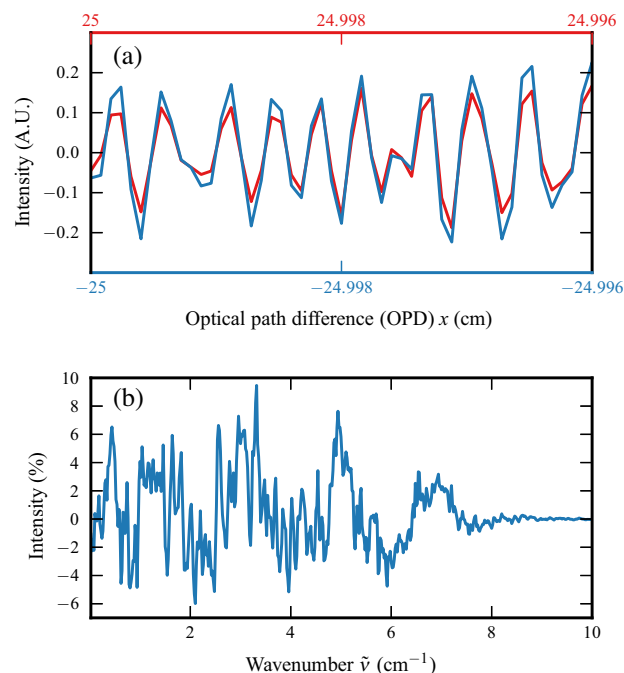


**Fig. 4.** The effects of simulated SIVs in the (a) OPD domain and (b) wavenumber domain. (a) Shows an SIV-perturbed interferogram that has had its DC level removed using  $V(x)$ , such that the regions of maximum OPD ( $-25 \text{ cm}$  and  $+25 \text{ cm}$ ) have the same DC level, but are no longer symmetric, containing spectral information from different altitudes. (b) Shows the low-wavenumber region of the Fourier transform of the same interferogram expressed as a percent of the mean peak amplitude. This region was zero-padded prior to simulating SIVs and can be high-pass filtered to obtain  $I_{\text{smooth}}(x)$ . Interferogram and spectrum are shown for low-dust conditions at 19.4 km.

Fig. 5 shows mean percent residuals comparing the SIV-perturbed spectra to the original synthetic spectra for each mitigation strategy. Means are taken between 20 and 75 km. Above 75 km, the residuals fall to zero, as there is little gas absorption, and are omitted from the mean to avoid biasing the amplitude. Below 20 km, many absorption lines reach zero transmission, leading to zero division in the fractional residuals. This is a larger problem in the high-dust scenario where the transmission baseline is reduced to below 1% in the high-wavenumber region. Fig. 5e and f use only spectra above 25 km and 30 km, respectively. At 30 km, orange in Fig. 2, the baseline level is below 0.002 near  $4000\text{ cm}^{-1}$ , and the small relative line depths in that region increase the percent residual. Mean percent residuals extending to 20 km are shown in grey for Fig. 5e and f and extend to  $-19\%$  and  $-14\%$ , respectively (note that this is the result of division by a small number, the residuals remain small).

In Fig. 5, the upper panels show the low-dust scenario, while the lower panels show the high-dust scenario. The light blue dashed lines in the lower panel indicate the y-axis limits of the upper panels, showing that when dust loading increases, the percent residuals are larger for all wavenumbers and for each mitigation strategy. In general, the residuals are very small, less than 0.25%, except for when absorption lines approach zero, due either to strong absorption, or to strong dust attenuation (e.g., Fig. 2). Residuals tend to be larger when the relative depth of absorption lines is greatest, peaking near 30 km. Higher in the atmosphere, gas absorption weakens, while lower in the atmosphere, dust attenuates the baseline. Because dust attenuation is weakest in the MCT detector wavenumber region, residuals remain large below 30 km. Residuals at all altitudes averaged in Fig. 5a and d are less than 1%, except near  $1350\text{ cm}^{-1}$ , which differs by up to 3% at lower altitudes.

The best performance is observed when  $I_{\text{smooth}}(x)$  is obtained from Method (iii), by convolving  $I_{\text{SIV}}(x)$  with Eq. (6) in the OPD domain, as in the slice-ipp software (dark blue in Fig. 5). The performance when  $I_{\text{smooth}}(x)$  is obtained by high-pass filtering in the wavenumber domain, Method (ii) (red in Fig. 5), is very similar, and the two methods were designed to be equivalent. When only the interferogram baseline is removed using the known  $V(x)$ , Method (i) (green in Fig. 5), we see the poorest performance, especially in the high-dust scenario at lower altitudes (Fig. 5e and f).

#### 4.2. VMR vertical profiles

The SNR of ACE-FTS is typically between 100 and 400 [2]. Noise levels in the spectra in regions without strong absorption lines are typically around 0.6%. The magnitude of the residuals between the SIV-perturbed spectra and the noise-free synthetic spectra presented here is generally smaller than typical noise levels of a real FTS.

Differences in the spectra on the order of 1%, or less, can have an effect on trace gas retrievals. Trace gas retrievals were performed on all three sets of SIV-perturbed spectra, and the original synthetic spectra using GGG. We applied MkIV microwindows and used the same *a priori* temperature, pressure, and gas VMR vertical profiles that we used to generate the synthetic spectra. Fig. 6 presents VMR vertical profile percent differences between retrievals from each of the SIV-perturbed spectra sets and the original synthetic spectra. Shown are  $\text{H}_2\text{O}$ ,  $\text{O}_3$ ,  $\text{CO}$ , and  $\text{CH}_4$ . Differences between the high- and low-dust scenarios increase as altitude decreases and dust levels increase. There are two large spikes in the  $\text{H}_2\text{O}$  VMR difference vertical profile and one in the  $\text{O}_3$  VMR difference vertical profile in the altitude range where spectral residuals are largest. These occur at inflection points in the *a priori* VMR

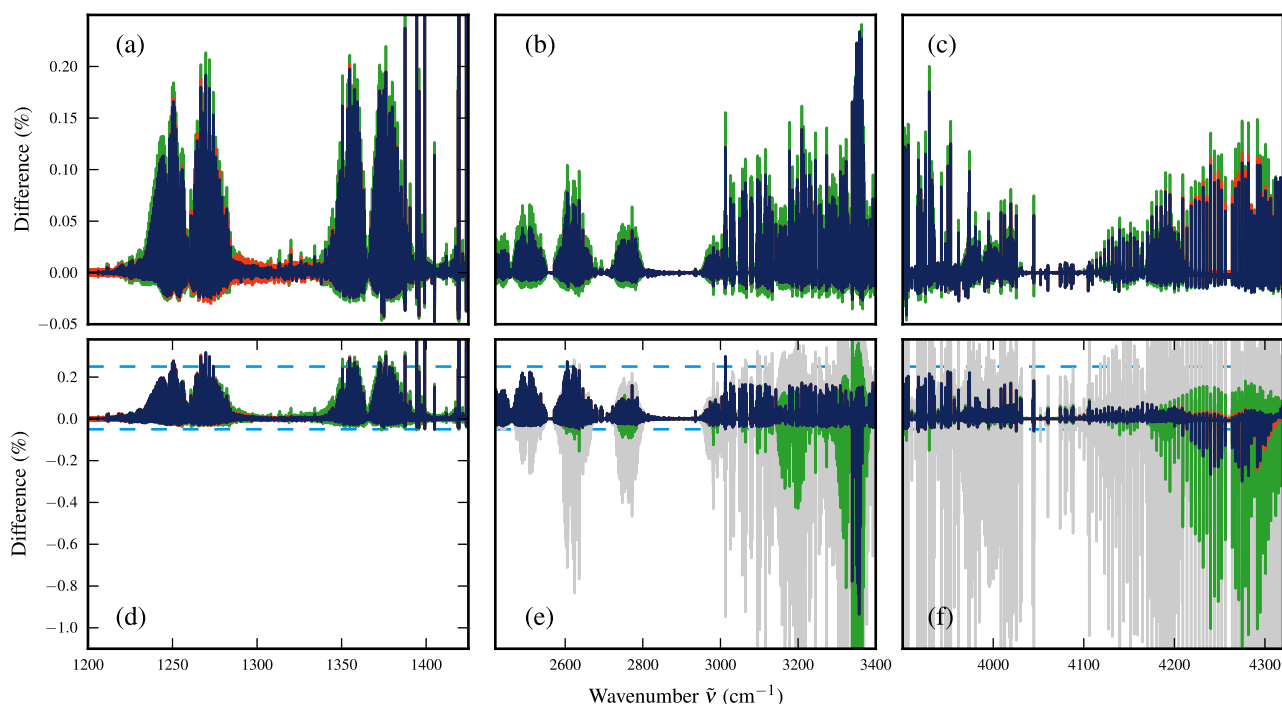
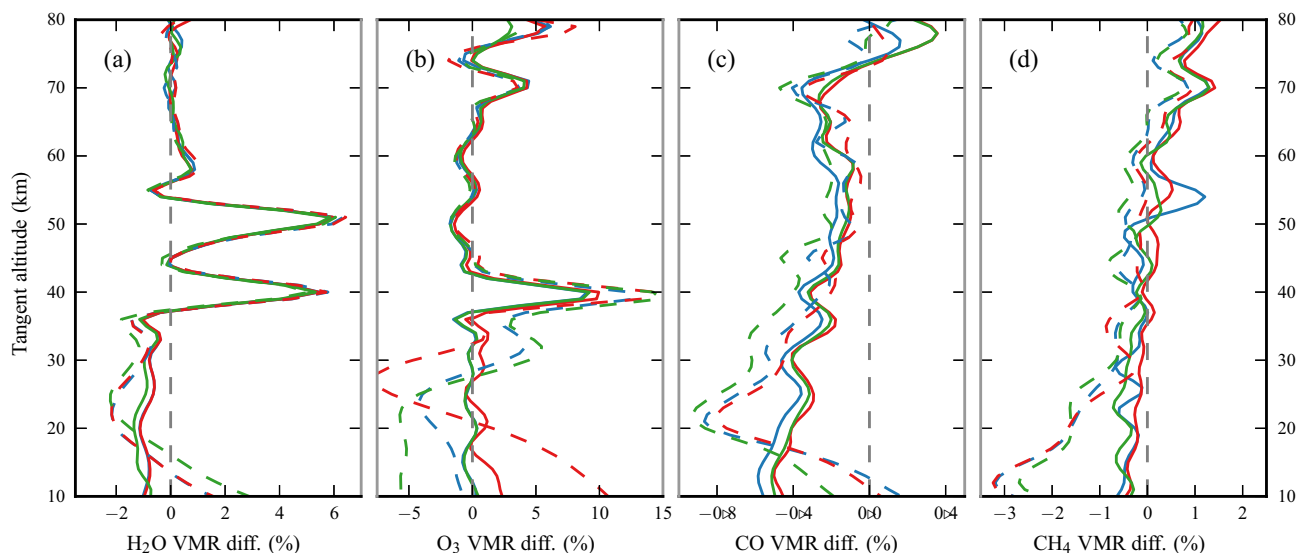


Fig. 5. Mean residuals between the SIV-perturbed spectra and the original synthetic spectra,  $I_{\text{corr}}(\bar{\nu}) - I(\bar{\nu})$ , after applying each mitigation technique. Residuals are expressed as a percentage of the original synthetic spectra, and shown are spectral regions where transmission does not approach zero: (a) and (d) are  $1200\text{--}1425\text{ cm}^{-1}$  in the MCT detector, (b) and (e) are  $2420\text{--}3400\text{ cm}^{-1}$  in the InSb detector, and (c) and (f) are  $3900\text{--}4320\text{ cm}^{-1}$  in the InSb detector. The upper panels, (a)–(c), are for low-dust conditions and the lower panels, (d)–(f) are for high-dust conditions. The dashed line (light blue) indicates the y-axis range of the low-dust panels. Means are taken over spectra between 20 and 75 km (20 spectra). Mitigation techniques use  $I_{\text{smooth}}(x)$  obtained by: Method (i) (green); Method (ii) (red); and Method (iii) (dark blue). In high-dust conditions, the baseline of the high-wavenumber spectral region rapidly approaches zero with decreasing altitude, so the minimum altitudes used in panel (e) and (f) are 25 km (16 spectra) and 30 km (18 spectra), respectively. The grey lines in panels (e) and (f) are of the mean residuals extending to 20 km when  $I_{\text{smooth}}(x)$  is obtained from  $V(x)$ .



**Fig. 6.** Differences between trace gas retrievals performed using SIV-perturbed and original synthetic spectra,  $\text{VMR}_{\text{corr}} - \text{VMR}_{\text{orig}}$ , expressed as a percentage of  $\text{VMR}_{\text{orig}}$ : (a)  $\text{H}_2\text{O}$ , (b)  $\text{O}_3$ , (c)  $\text{CO}$ , (d)  $\text{CH}_4$ . SIV perturbations are mitigated with  $I_{\text{smooth}}(x)$  obtained by: Method (i), using known  $V(x)$  (green); Method (ii), high-pass filtering in the wavenumber domain, as in Keppel-Aleks et al. [12] (red); and Method (iii), high-pass filtering in the OPD domain with a convolution operation (dark blue). Low-dust conditions are solid lines, high-dust conditions are dashed lines.

vertical profiles for those gases where the change in VMR between tangent altitudes is largest.

The closest agreement between SIV-perturbed spectra and the original spectra is for  $\text{CO}$ , which has the largest VMR among the gases presented. Retrievals from the high-dust spectra deviate below 30 km, and their percent difference is double those from the low-dust spectra, but remains below 1%.  $\text{CH}_4$  retrievals also have very small VMR differences, and show large deviations between high- and low-dust scenarios below 30 km, but have a higher magnitude, with VMR differences for the high-dust scenario reaching 3% near 20 km. Low-dust scenario VMR differences remain below 1%. Between the two dust scenarios and three SIV mitigation techniques, obtaining  $I_{\text{smooth}}(x)$  following Keppel-Aleks et al. [12] (Method (ii)) often has the smallest VMR differences, while using the known  $V(x)$  to obtain  $I_{\text{smooth}}(x)$  (Method (i)) tends to result in the largest VMR differences. However, differences between methods are small, and no method is consistently better or worse at all altitudes.

The  $\text{H}_2\text{O}$  and  $\text{O}_3$  VMR differences in the low-dust scenario are similar, below 2%, except where there are spikes. The high-dust scenario deviates strongly below 30 km for all SIV mitigation strategies, where the VMRs of  $\text{H}_2\text{O}$  and  $\text{O}_3$  are large. VMR differences from mitigation using Method (iii), are similar to those obtained by using Method (ii) for  $\text{H}_2\text{O}$ , and Method (i) for  $\text{O}_3$ .

Noise was added to the spectra to test the retrieval sensitivity. Two noise sources were applied: extracting noise from spectra recorded by ACE-FTS, and generating random noise based on ACE-FTS spectra. The typical noise in an ACE-FTS spectrum can be measured using spectra recorded at the start or end of an occultation, where there can be no discernible gas absorption at high altitudes, or no solar transmission near the ground, or from spectra recorded while observing deep space. ACE-FTS noise spectra can be added directly to synthetic spectra, or we can assume the noise follows a Gaussian distribution, measure Gaussian parameters from the spectra, and generate random noise to add to synthetic spectra. The noise observed in ACE-FTS spectra is not normally distributed, however, and the amplitude varies with wavenumber [2], so using noise recorded by ACE-FTS is preferred.

The magnitude of the VMR differences in Fig. 6 is much smaller than for differences between retrievals from the original synthetic spectra and those spectra with noise added; these differences oscillate between  $\pm 5\%$ , but can be larger than 10% at some altitudes. VMR differences for noisy spectra are also much larger at high altitudes, where absorption line depth is reduced to the same magnitude as the noise level.

## 5. Discussion

Keppel-Aleks et al. [12] distinguish between grey (absorbed equally at all wavelengths) and non-grey SIVs, correctly identifying the limitation of Method (ii) when the SIV strength is wavenumber-dependent. They applied and evaluated their filter on non-grey SIVs measured by a ground-based interferometer, then simulated low-amplitude grey SIVs that may be encountered by a ground-based FTS on Earth. They found that the correction was less effective for the grey dataset than non-grey, but still within the tolerance set by TCCON. The SIVs presented here are much stronger, and intended to investigate the limits of the TCCON correction method presented in Keppel-Aleks et al. [12] for application to the dusty Martian atmosphere. These SIVs differ by the inclusion of dust, increased optical path length, reduced spectral resolution, and larger relative DC levels of consecutive spectra.

The SIVs we have simulated result in a sloped DC level in the interferograms that must be removed before a Fourier transform is performed, otherwise distortions will appear in the target spectral region. The method presented by Keppel-Aleks et al. [12] cannot correct for these SIVs by high-pass filtering the spectra. However, the technique currently applied by TCCON, which smooths the interferogram in the OPD domain, effectively corrects these strong, grey SIVs. The quality of the correction depends on the type of smoothing algorithm used, which may not effectively remove the centreburst amplitude, or affect the spectral information at high OPD.

Ridder et al. [20] identified an issue with the Keppel-Aleks et al. [12] method in the mid-infrared range where an MCT detector is used, as on ACE-FTS and future ACE-FTS-like instruments. The ADCs used by MCT detectors apply an unknown voltage offset to

the signal which adds to the DC level of the interferogram. Ridder et al. [20] present two methods to measure and remove the unknown offset, and evaluate their effectiveness using ground-based FTSs on Earth. In one case, they measured the offset by recording two consecutive interferograms using an MCT detector, and determined the offset by equating their modulation efficiencies, as in Eq. (1) with the offset added to the denominator. In the other case, the modulation efficiency was measured using an InSb detector and assumed to be equal for both detectors. Since an ACE-FTS-like instrument will use MCT and InSb detectors, and interferograms will be acquired continuously, both methods will be applicable, while the modulation efficiency can be characterized and monitored. Furthermore, the offset can be measured directly when interferograms of deep space are recorded between occultations.

Stronger SIVs were created by altering the *a priori* dust mole fraction vertical profiles used to generate synthetic spectra for the high-dust scenario (Fig. 1). When comparing different mitigation techniques, results are similar to the original high- and low-dust scenarios, where Methods (ii) and (iii) achieve close to the same performance, and Method (i) performs slightly worse. The effects of the simulation on spectra are also similar to the high-dust simulation, and can be seen in the spectral residuals shown in Fig. 7, which is the same as Fig. 5d, but compares the four dust scenarios rather than mitigation techniques. Fig. 7 shows mean spectral residuals for synthetic spectra before and after mitigation using Method (iii) in the MCT region for the following dust scenarios: a detached layer of dust, high-dust, high-dust with stratification, and low-dust. Relative to spectral residuals from the high-dust scenario, a strong detached layer decreases the similarity of perturbed spectra to the original spectra, while introducing stratification produces results similar to the low-dust scenario. This is partially due to the density of observations, which can reduce the amount dust can change over a single observation. The rates of change of pressure and density with altitude produce a more dominant effect, however. When we introduce stratification, and decrease or increase the dust loading at a given altitude relative to the high-dust scenario, the dust extinction along the optical path still varies monotonically because the change in the total column of dust along the line-of-sight is greater than

the change in dust mole fraction. Furthermore, when computing synthetic spectra, GGG does not distinguish local dust clouds, so layers of increased dust loading are global, and every observation at lower altitudes passes through those layers. With respect to Fig. 5, the effect of introducing stratification is to reduce the percent differences, as we have reduced the total dust, moving the simulation closer to the low-dust scenario. The effect of a detached layer is greater, as it causes the strongest vertical gradient of dust loading, and produces the largest mean spectral differences throughout the wavenumber region of the MCT and InSb detectors. The detached layer simulated here, however, contains a higher dust content than observations of the Martian atmosphere support (e.g., [10,9]).

## 6. Conclusions

A solar occultation FTS similar to the Earth-observing ACE-FTS is ideally suited to detecting unknown trace gases in the Martian atmosphere and retrieving their VMR vertical profiles. Dust storms elevate the dust content of the Martian atmosphere, scattering and absorbing transmitted solar radiation. A problem faced by an ACE-FTS-like mission to Mars is that the dust level through the optical path can vary strongly during the acquisition of each interferogram. We simulated transmission spectra and interferograms for the Martian atmosphere, and perturbed them with SIVs to evaluate whether these perturbations can be effectively mitigated.

Mean residuals between the original synthetic spectra and those perturbed with, and corrected for, an SIV with each of the three methods are below 0.25% between 20 and 75 km for both high- and low-dust conditions at most wavenumbers, except above 3000  $\text{cm}^{-1}$  and below 30 km in the high-dust scenario. The residual magnitudes are smaller than the typical noise levels of ACE-FTS, which are around 0.6% for an SNR of 100–400. Such small differences in the spectra do affect trace gas retrievals, and we investigated  $\text{H}_2\text{O}$ ,  $\text{O}_3$ ,  $\text{CO}$  and  $\text{CH}_4$  in this study. The percent differences in VMR vertical profiles retrieved from each set of perturbed spectra and the original spectra was largest for  $\text{H}_2\text{O}$  and  $\text{O}_3$ , peaking at 6% and 10%, at inflection points in their vertical profiles where there are large changes in VMR between layers. Otherwise, differences remain below 2%. The  $\text{CO}$  VMR differences are below 0.5% and the  $\text{CH}_4$  VMR differences are below 1%. The high-dust scenario most strongly affects the lower altitudes (below 40 km), as there is very little suspended dust or gas above 60 km in either scenario, and the high-dust VMR vertical profiles diverge from the low-dust profiles with decreasing altitude. The spectral differences caused by simulating, then mitigating, SIVs affect VMR vertical profile retrievals less significantly than adding noise to the spectra.

While all three SIV mitigation methods perform well, as seen in Figs. 5 and 6, it should be stressed that only the Method (iii) used by slice-ipp is applicable to a future ACE-FTS-like mission. The high-pass filter described in Keppel-Aleks et al. [12] cannot effectively mitigate the SIVs simulated here, because the perturbation affects the entire wavenumber range. The results shown in Figs. 5 and 6 required additional processing steps that required knowledge of how the SIV perturbation was created. Method (i), where a fit to known  $V(x)$  is used to remove the interferogram baseline is also not applicable to future missions since it requires accurately measuring  $V(x)$  at the centreburst location and assumes the SIV is smooth throughout acquisition. SIV mitigation using Method (iii), where  $I_{\text{smooth}}(x)$  is obtained by a high-pass filter in OPD space through a convolution operation, currently applied by the slice-ipp software, will be suitable for performing trace gas retrievals at Mars using an ACE-FTS-like instrument on a future mission.

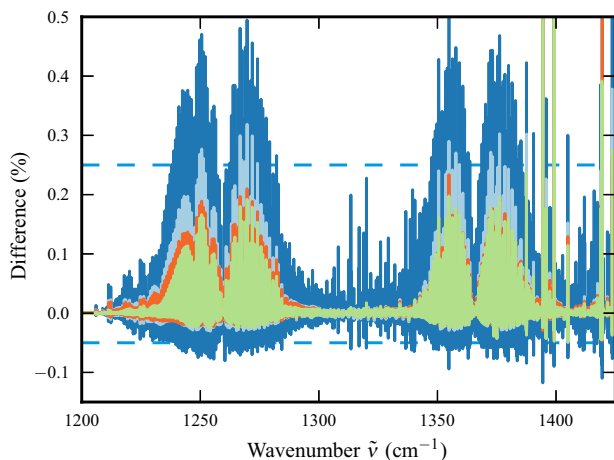


**Fig. 7.** Comparison of the mean spectral residuals caused by varying the *a priori* dust profile used to generate synthetic spectra. Each residual is the mean of the difference between the original synthetic spectra and the dust-perturbed spectra mitigated using  $I_{\text{smooth}}(x)$  obtained from Method (iii). Means are taken over an altitude range of 20–75 km (20 spectra) and the wavenumber region shown is 1200–1425  $\text{cm}^{-1}$  in the MCT detector, as in Fig. 5a and d. Dust scenarios are: a detached layer (blue), high-dust (light blue), stratified dust (orange), and low-dust (green).

## Acknowledgements

Funding for this project was provided by the CSA and the Natural Sciences and Engineering Research Council of Canada (NSERC). We would like to thank the ACE Science Team for providing Level 1 data (spectra), Level 0 data (raw interferograms), and for their help and input throughout the project. We want to thank collaborators on MATMOS and members of TCCON for guidance with GGG.

## References

- [1] P.F. Bernath, C.T. McElroy, M.C. Abrams, C.D. Boone, M. Butler, C. Camy-Peyret, M. Carleer, C. Clerbaux, P.F. Coheur, R. Colin, P. DeCola, M. DeMazière, J.R. Drummond, D. Dufour, W.F.J. Evans, H. Fast, D. Fussen, K. Gilbert, D.E. Jennings, E.J. Llewellyn, R.P. Lowe, E. Mahieu, J.C. McConnell, M. McHugh, S.D. McLeod, R. Michaud, C. Midwinter, R. Nassar, F. Nichitiu, C. Nowlan, C.P. Rinsland, Y.J. Rochon, N. Rowlands, K. Semeniuk, P. Simon, R. Skelton, J.J. Sloan, M.A. Soucy, K. Strong, P. Tremblay, D. Turnbull, K.A. Walker, I. Walkty, D.A. Wardle, V. Wehrle, R. Zander, J. Zou, Atmospheric chemistry experiment (ACE): mission overview, *Geophys. Res. Lett.* 32 (2005) L15S01, <http://dx.doi.org/10.1029/2005GL022386>.
- [2] C.D. Boone, R. Nassar, K.A. Walker, Y. Rochon, S.D. McLeod, C.P. Rinsland, P.F. Bernath, Retrievals for the atmospheric chemistry experiment Fourier-transform spectrometer, *Appl. Opt.* 44 (2005) 7218–7231, <http://dx.doi.org/10.1364/AO.44.007218>.
- [3] J.W. Brault, Fourier transform spectroscopy, in: A.O. Benz, M. Huber, M. Mayor (Eds.), *High Resolution in Astronomy, Swiss Society of Astronomy and Astrophysics, Sauverny, Switzerland, 1985*, pp. 3–61.
- [4] B.A. Cantor, P.B. James, W.M. Calvin, MARCI and MOC observations of the atmosphere and surface cap in the north polar region of Mars, *Icarus* 208 (2010) 61–81, <http://dx.doi.org/10.1016/j.icarus.2010.01.032>.
- [5] J. Dodion, D. Fussen, F. Vanhellemont, C. Bingen, N. Matshvili, K. Gilbert, R. Skelton, D. Turnbull, S.D. McLeod, C.D. Boone, K.A. Walker, P.F. Bernath, Cloud detection in the upper troposphere-lower stratosphere region via ACE imagers: a qualitative study, *J. Geophys. Res.* 112 (2007) D03208, <http://dx.doi.org/10.1029/2006JD007160>.
- [6] D. Doeringer, A. Eldering, C.D. Boone, G. González Abad, P.F. Bernath, Observation of sulfate aerosols and SO<sub>2</sub> from the Sarychev volcanic eruption using data from the atmospheric chemistry experiment (ACE), *J. Geophys. Res.* 117 (2012) D03203, <http://dx.doi.org/10.1029/2011JD016556>.
- [7] M.N. Eremenko, A.Y. Zasetsky, C.D. Boone, J.J. Sloan, Properties of high-altitude tropical cirrus clouds determined from ACE FTS observations, *Geophys. Res. Lett.* 32 (2005) L15S07, <http://dx.doi.org/10.1029/2005GL022428>.
- [8] V. Formisano, F. Angrilli, G. Arnold, S. Atréya, G. Bianchini, D. Biondi, A. Blanco, M.I. Blecka, A. Coradini, L. Colangeli, A. Ekonomov, F. Esposito, S. Fonti, M. Giuranna, D. Grassi, V. Gnediykh, A. Grigoriev, G. Hansen, H. Hirsh, I. Khatuntsev, A. Kiselev, N. Ignatiev, A. Jurewicz, E. Lellouch, J. Lopez Moreno, A. Marten, A. Mattana, A. Maturilli, E. Mencarelli, M. Michalska, V. Moroz, B. Moshkin, F. Nespoli, Y. Nikolsky, R. Orfei, P. Orleanski, V. Orofino, E. Palomba, D. Patsaev, G. Piccioni, M. Rataj, R. Rodrigo, J. Rodriguez, M. Rossi, B. Saggin, D. Titov, L. Zasova, The planetary Fourier spectrometer (PFS) onboard the European Mars Express mission, *Planet Space Sci.* 53 (2005) 963–974, <http://dx.doi.org/10.1016/j.pss.2004.12.006>.
- [9] S.D. Guzewich, E.R. Talaat, A.D. Toigo, D.W. Waugh, T.H. McConnochie, High-altitude dust layers on Mars: observations with the thermal emission spectrometer, *J. Geophys. Res.* 118 (2013) 1177–1194, <http://dx.doi.org/10.1002/jgre.20076>.
- [10] N.G. Heavens, M.I. Richardson, A. Kleinböhl, D.M. Kass, D.J. McCleese, W. Abdou, J.L. Benson, J.T. Schofield, J.H. Shirley, P.M. Wolkenberg, The vertical distribution of dust in the Martian atmosphere during northern spring and summer: observations by the Mars Climate Sounder and analysis of zonal average vertical dust profiles, *J. Geophys. Res.* 116 (2011) 4003, <http://dx.doi.org/10.1029/2010JE003691>.
- [11] M.N. Izakov, The Martian upper atmosphere structure from the Viking spacecraft experiments, *Icarus* 36 (1978) 189–197, [http://dx.doi.org/10.1016/0019-1035\(78\)90103-3](http://dx.doi.org/10.1016/0019-1035(78)90103-3).
- [12] G. Keppel-Aleks, G.C. Toon, P.O. Wennberg, N.M. Deutscher, Reducing the impact of source brightness fluctuations on spectra obtained by Fourier-transform spectrometry, *Appl. Opt.* 46 (2007) 4774–4779, <http://dx.doi.org/10.1364/AO.46.004774>.
- [13] A. Kleinert, G. Aubertin, G. Perron, M. Birk, G. Wagner, F. Hase, H. Nett, R. Poulin, MIPAS level 1B algorithms overview: operational processing and characterization, *Atmos. Chem. Phys.* 7 (2007) 1395–1406, <http://dx.doi.org/10.5194/acp-7-1395-2007>.
- [14] O. Korablev, A. Trokhimovsky, A.V. Grigoriev, A. Shakun, Y.S. Ivanov, B. Moshkin, K. Anufreychik, D. Timonin, I. Dziuban, Y.K. Kalinnikov, F. Montmessin, Three infrared spectrometers, an atmospheric chemistry suite for the ExoMars 2016 trace gas orbiter, *J. Appl. Remote Sens.* 8 (2014) 084983, <http://dx.doi.org/10.1117/1.JRS.8.084983>.
- [15] A. Kuze, H. Suto, K. Shiomi, T. Urabe, M. Nakajima, J. Yoshida, T. Kawashima, Y. Yamamoto, F. Kataoka, H. Buijs, Level 1 algorithms for TANSO on GOSAT: processing and on-orbit calibrations, *Atmos. Meas. Tech.* 5 (2012) 2447–2467, <http://dx.doi.org/10.5194/amt-5-2447-2012>.
- [16] G.F. Lindal, H.B. Hotz, D.N. Sweetnam, Z. Shippony, J.P. Brenkle, G.V. Hartsell, R. T. Spear, Viking radio occultation measurements of the atmosphere and topography of Mars – data acquired during 1 Martian year of tracking, *J. Geophys. Res.* 84 (1979) 8443–8456, <http://dx.doi.org/10.1029/JB084iB14p08443>.
- [17] D.J. McCleese, N.G. Heavens, J.T. Schofield, W.A. Abdou, J.L. Bandfield, S.B. Calcutt, P.G.J. Irwin, D.M. Kass, A. Kleinböhl, S.R. Lewis, D.A. Paige, P.L. Read, M. I. Richardson, J.H. Shirley, F.W. Taylor, N. Teanby, R.W. Zurek, Structure and dynamics of the Martian lower and middle atmosphere as observed by the Mars Climate Sounder: seasonal variations in zonal mean temperature, dust, and water ice aerosols, *J. Geophys. Res.* 115 (2010) E12016, <http://dx.doi.org/10.1029/2010JE003677>.
- [18] L. Mertz, Auxiliary computation for fourier spectrometry, *Infrared Phys.* 7 (1967) 17–23, [http://dx.doi.org/10.1016/0020-0891\(67\)90026-7](http://dx.doi.org/10.1016/0020-0891(67)90026-7).
- [19] C. Petri, T. Warneke, N. Jones, T. Ridder, J. Messerschmidt, T. Weinzierl, M. Geibel, J. Notholt, Remote sensing of CO<sub>2</sub> and CH<sub>4</sub> using solar absorption spectrometry with a low resolution spectrometer, *Atmos. Meas. Tech.* 5 (2012) 1627–1635, <http://dx.doi.org/10.5194/amt-5-1627-2012>.
- [20] T. Ridder, T. Warneke, J. Notholt, Source brightness fluctuation correction of solar absorption fourier transform mid infrared spectra, *Atmos. Meas. Tech.* 4 (2011) 1045–1051, <http://dx.doi.org/10.5194/amt-4-1045-2011>.
- [21] C.E. Sioris, C.D. Boone, P.F. Bernath, J. Zou, C.T. McElroy, C.A. McLinden, Atmospheric chemistry experiment (ACE) observations of aerosol in the upper troposphere and lower stratosphere from the Kasatochi volcanic eruption, *J. Geophys. Res.* 115 (2010) D00L14, <http://dx.doi.org/10.1029/2009JD013469>.
- [22] G.C. Toon, The JPL MkIV interferometer, *Opt. Photon. News* 2 (1991) 19–21, <http://dx.doi.org/10.1364/OPN.2.10.000019>.
- [23] G.C. Toon, B. Sen, A. Kleinböhl, Derivation of Pseudo-lines from Laboratory Cross-sections, 2006. <mark4sun.jpl.nasa.gov/pseudo.html>.
- [24] T. Warneke, A.K. Petersen, C. Gerbig, A. Jordan, C. Rödenbeck, M. Rothe, R. Macatangay, J. Notholt, O. Schrems, Co-located column and in situ measurements of CO<sub>2</sub> in the tropics compared with model simulations, *Atmos. Chem. Phys.* 10 (2010) 5593–5599, <http://dx.doi.org/10.5194/acp-10-5593-2010>.
- [25] D. Wunch, G.C. Toon, J.L. Blavier, R.A. Washenfelder, J. Notholt, B.J. Connor, D. W.T. Griffith, V. Sherlock, P.O. Wennberg, The total carbon column observing network, *Philos. Trans. R. Soc. A* 369 (2011) 2087–2112, <http://dx.doi.org/10.1098/rsta.2010.0240>.